

A General Synthesis Strategy for Monodisperse Metallic and Metalloid Nanoparticles (In, Ga, Bi, Sb, Zn, Cu, Sn, and Their Alloys) via in Situ Formed Metal Long-Chain Amides

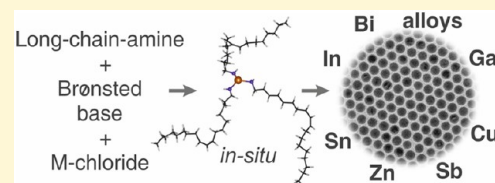
Meng He,^{†,‡} Loredana Protesescu,^{†,‡} Riccarda Caputo,^{†,‡} Frank Krumeich,[†] and Maksym V. Kovalenko^{*,†,‡}

[†]Institute of Inorganic Chemistry, Department of Chemistry and Applied Biosciences, ETH Zürich, CH-8093 Zürich, Switzerland

[‡]Empa-Swiss Federal Laboratories for Materials Science and Technology, CH-8600 Dübendorf, Switzerland

Supporting Information

ABSTRACT: We report a facile one-pot synthesis of highly monodisperse nanoparticles (5–30 nm in diameter, 5–10% in standard size distribution) of various metals and metalloids such as In, Sn, Bi, Sb, Ga, Cu, Zn, and their alloys (Cu_6Sn_5 , Cu_2Sb , $\text{Bi}_{x}\text{Sb}_{1-x}$ etc.) using inexpensive commercial precursors. Several of these metals and alloys had not been previously obtained in the form of uniform nanoparticles. The proposed reaction mechanism has been elucidated with multinuclear (^1H , ^7Li , ^{19}Sn) NMR spectroscopy combined with DFT and molecular dynamics simulations. Metal chloride is reacted with long-chain primary or secondary amine such as oleylamine and dioctylamine in the presence of a strong Brønsted base that deprotonates the amine and thus promotes the formation of metal long-chain amide. The in situ formed amide is then reduced or thermally decomposed into corresponding metal nanoparticles. This simple methodology eliminates elaborate preparation, storage, and handling of highly reactive, moisture and oxygen sensitive molecular precursors of these metals, while providing a compelling quality of nanomaterials.



INTRODUCTION

Colloidal synthesis of inorganic nanoparticles (NPs), which are usually crystalline (nanocrystals, NCs), opened access to a variety of nanomaterials with unprecedented characteristics such as precise size-tuning in the range of 2–100 nm, narrow size distributions of just several %, isotropic and anisotropic shapes,^{1–7} compositional gradients,^{4,6,8–10} and core–shell morphologies.¹¹ Over the last 10–20 years, these nanomaterials have advanced our understanding and control of the effects of size-quantization, shape, and surface on fundamental optical, electronic, magnetic, plasmonic, and catalytic properties.¹ Consequently, NPs are now actively pursued for applications in solid-state devices such as solar cells,¹² light-emitting diodes,¹³ photodetectors,^{14–16} thermoelectrics,^{17,18} transistors,^{16,19} and integrated electronic circuits,^{20,21} as well as for electrochemical energy storage^{22–25} and catalysis.⁷

When a new chemical synthesis of a colloidal nanomaterial is targeted, the most critical and difficult task is rational selection of molecular precursors.^{1–7,26} At the early trial-and-error stage researchers often spend most of their time trying to identify the best-suited combination of precursors, capping ligands, and solvents. Besides yielding a highly pure target compound without undesired side reactions and impurities, compelling precursors have to provide the ability to independently tune the rate of the nucleation and growth of NPs and must be soluble in and nonreactive toward organic solvents (usually high-boiling, nonpolar), stable at room temperature but reactive at elevated temperatures, and, very importantly, easily accessible commer-

cially or via well-documented and simple preparation. Thus far, most commonly used are M–O bonded precursors (e.g., carboxylates, alcoholates, or acetylacetones),^{27–29} organometallic precursors (e.g., carbonyl-, alkyl- or cyclopentadienyl compounds and similar),^{30–33} and M–Si bonded compounds such as trimethylsilyl derivatives.³⁴

Particularly suitable for obtaining highly reduced materials such as metallic and metalloid NPs²⁶ are metal–nitrogen bonded precursors, such as well-known homoleptic metal and metalloid alkylamides $\text{M}(\text{NR}_2)_n$ and silylamides $\text{M}[\text{N}(\text{SiMe}_3)_2]_n$. The key benefits of these amides are the high reactivity of single element–nitrogen bonds, absence of oxygen atoms (e.g., no risk of metal–oxide formation), and facile thermal decomposition or reduction as well as various oxidation and metathesis pathways due to the polar character of M–N bonds. Alkyl- and silylamides have been extensively studied from the 1950s and presently are known for most metals and metalloids.³⁵ Their use for NP synthesis has been pioneered by Chaudret et al. in the early 2000s (Sn, Fe, Co, Fe–Co, Fe–Ni, Fe–oxides)^{36–43} and then extended by us and by others to various materials such as Ga,⁴⁴ Bi,^{45–48} $\text{Bi}_{1-x}\text{Sb}_x$,⁴⁹ Pb,⁵⁰ In,⁵¹ Sn/SnO₂,^{25,52} CuTe,⁵³ InSb,⁵⁴ Ag₂Se,⁵⁵ and SnTe⁵⁶ NPs (nonexhaustive list). However, an important shortcoming of metal amides as precursors, rooted in their excellent reactivity, is that they are extremely air- and moisture-sensitive or even

Received: December 9, 2014

Revised: December 19, 2014

Published: December 19, 2014

flammable and often require elaborate synthesis, isolation, and handling procedures. Some amides such as $\text{Sn}(\text{NMe}_2)_2$ and $\text{Bi}[\text{N}(\text{SiMe}_3)_2]_3$ are also highly light sensitive. Those silyl- and alkylamides which are available commercially as precursors for atomic layer deposition or chemical vapor deposition are often exceedingly expensive for colloidal NP synthesis.

Modern synthesis of NCs requires clear understanding of the precursor-to-NC reaction pathways, high atomic economy, and facile experimental realization, while providing compelling quality of the product (uniform and tunable morphologies and compositions). From the viewpoint of practical chemistry of nanomaterials, particularly attractive might be a one-pot synthesis in which the actual metal–nitrogen bonded precursor is formed *in situ*. In a number of recent reports, monodisperse NPs (Bi , Pb , CuTe)^{57–59} were obtained by combining $\text{LiN}(\text{SiMe}_3)_2$ with corresponding metal chloride (or similar inorganic salt) and reducing agent or chalcogen precursor. These $\text{MCl}_n + \text{LiN}(\text{SiMe}_3)_2 + [\text{H}, \text{O}, \text{S}, \text{Se}] \rightarrow \text{NPs}$ reactions are often conducted in the primary amine such as oleylamine, and we recently became aware that the actual precursor may not necessarily be $\text{M}[\text{N}(\text{SiMe}_3)_2]_n$, but a M–oleylamido complex, $\text{M}(\text{RNH})_n$.^{24,25} The role of $\text{LiN}(\text{SiMe}_3)_2$ is to act as a base for (partial) deprotonation of primary amine RNH_2 , thus promoting the formation of $\text{M}(\text{RNH})_n$ species (monomeric or oligomeric).

In this work we thought to obtain detailed mechanistic insight and further elaborate the idea of using metal–oleylamido complexes, and more generally metal long-chain amides, as *in situ* formed, highly reactive metal and metalloid precursors. We thus propose a generalized, very simple one-pot synthesis methodology for preparing high-quality inorganic NPs, fully based on inexpensive commercial precursors. In particular, we show that *n*-butyllithium (*n*-BuLi) provides this shortcut by promoting the formation of M–oleylamido complexes. Through the detailed study by multinuclear magnetic resonance (^1H , ^{7}Li , ^{119}Sn NMR) spectroscopy we have traced the Brønsted acid–base reaction and *in situ* formation of M–oleylamide species. In particular, we confirm that the underlying reaction pathway is identical for both *n*-BuLi and for $\text{LiN}(\text{SiMe}_3)_2$ and for other studied organic bases. The role of the long-chain-amide ligand is not only to form a reactive M–N bond but also to act as surfactant right from the early stages of nucleation, as commonly assumed for the role of long chain carboxylates such as oleate in the synthesis of carboxylate-capped NPs from metal carboxylates as precursors.⁶⁰ We then have synthesized highly monodisperse NPs (5–30 nm, 5–10% standard size distribution) of a variety of metals and metalloids (In , Sn , Ga , Bi , Sb , Zn , Cu) and their alloys ($\text{Bi}_x\text{Sb}_{1-x}$, Cu_2Sb , Cu_6Sn_5). Of these materials, highly uniform colloidal Zn , Cu_2Sb , and Cu_6Sn_5 NPs have never been reported before. When *in situ* formed oleylamine is not sufficiently reactive, as in the case of Ga , an *in situ* formed secondary amide precursor ($\text{Ga(III)}-\text{dioctylamide}$) can be successfully utilized for producing highly uniform Ga NPs.

EXPERIMENTAL SECTION

Chemicals and Solvents. Indium(III) chloride (99.999%, Sigma-Aldrich), gallium chloride (99.999%, ABCR), bismuth(III) chloride (99.999%, Sigma-Aldrich), copper(II) chloride (99.995%, Aldrich), antimony(III) chloride (99.999%, ABCR), tin(II) chloride (anhydrous, ABCR), zinc chloride (anhydrous, beads, 99.99%, Sigma-Aldrich), gallium chloride (99.999%, ABCR), dioctylamine (DOA, 98%, Sigma-Aldrich), *n*-butyllithium in heptanes (*n*-BuLi, 2.7 M, Aldrich), lithium bis(trimethylsilyl)amide [$\text{LiN}(\text{SiMe}_3)_2$, 97%, Sigma-Aldrich], lithium dimethylamide (LiNMe_2 , 95%, Sigma-Aldrich), lithium diisopropylamide ($\text{LiN}(\text{iPr})_2$, 97%, Sigma-Aldrich), oleylamine (OLA, tech., TCI),

1-dodecanethiol (DT, 98%, Sigma-Aldrich), trioctylphosphine (TOP, 97%, STREM), oleic acid (OA, 90%, Aldrich), lithium triethylborohydride (“superhydride”, LiEt₃BH, 1 M in THF, Aldrich), diisobutylaluminum hydride solution (DIBAH, 1 M in toluene, Sigma-Aldrich), octadecene (ODE, 90%, Sigma-Aldrich), dioctylamine (DOA, 98%, Sigma-Aldrich), toluene (99.9%, Sigma-Aldrich), ethanol (\geq 99.9%, Scharlau) and dried ethanol (max. 0.01% H_2O , VWR Merck), and toluene (\geq 99.9%, max. 0.005% H_2O , VWR Merck) were used as received. OLA was additionally dried at 100 °C under vacuum.

All syntheses were carried out using Schlenk line under nitrogen atmosphere; isolation and purification of NPs were carried out in air (except for Zn NPs). Detailed screening of common reaction parameters (temperatures, concentrations of reactants) has led to broad size-tunability for all studied NPs, as extensively illustrated in Tables S1–S20 in Supporting Information containing all experimental details and corresponding TEM images.

Synthesis of Indium NPs (*n*-BuLi based). In a typical synthesis of 22 nm In NPs, dried OLA (13 mL) was mixed with InCl_3 (0.028 g, 0.125 mmol) in a 50 mL three neck flask, additionally dried under vacuum (45 min at 100 °C), and heated to 160 °C under nitrogen, followed by the injection of *n*-BuLi (3.6 mmol, 1.33 mL, 2.7 M in heptane) and, 10 s after, by injection of superhydride (0.3 mmol, 0.3 mL, 1 M in THF). In ~10 s, the reaction was quenched by injecting anhydrous toluene (12 mL) and cooling with an ice–water bath. At 50 °C, dried OA (0.4 mL) was added to displace weakly bound oleylamine/oleylamine ligand capping. Indium NPs were precipitated by ethanol (25 mL), separated by centrifugation, redispersed in toluene (5 mL) containing OA (100 μL), and then once again precipitated by ethanol and redispersed in toluene. The size of In NPs can be tuned in 7–22 nm range by adjusting the concentrations of InCl_3 and superhydride and by reaction time.

Synthesis of Bismuth NPs (*n*-BuLi Based). The same procedure as for In NPs has been followed, using BiCl_3 , but without any reducing agent. Furthermore, drying of BiCl_3 and OLA was conducted at 60 °C for only 20 min in order to avoid reduction of Bi.

Synthesis of Sn NPs (*n*-BuLi Based). The same procedure as for In NPs has been followed, using SnCl_2 as precursor and DIBAH as reducing agent.

Synthesis of Sb NPs (*n*-BuLi Based). In a typical synthesis of 11 nm Sb NPs, TOP (9 mL) and dried OLA (3 mL) were loaded into 50 mL three neck flask and heated to 160 °C, followed by the injection of *n*-BuLi (3.6 mmol, 1.33 mL, 2.7 M in heptane) and, in 10 s, by injection of SbCl_3 /toluene solution (0.125 mmol/1 mL). After 30 s, the reaction was quenched by injecting dried toluene (12 mL). Isolation and purification procedures were analogous to those of In NPs, except for the use of OA/DT mixture (1:1) as ligands added during the cooling of reaction mixture.

Synthesis of Copper NPs (*n*-BuLi Based). The same procedure as for In NPs has been followed using CuCl_2 as precursor, but without addition of reducing agents.

$\text{LiN}(\text{SiMe}_3)_2$ Based Syntheses of In, Bi, and Cu NPs. The synthetic procedures were the same as for *n*-BuLi based syntheses but replacing *n*-BuLi by the same molar amount of $\text{LiN}(\text{SiMe}_3)_2$ (3.6 mmol dissolved in 2 mL of dried toluene).

Synthesis of $\text{Bi}_x\text{Sb}_{1-x}$ NPs. In a typical synthesis of 12 nm $\text{Bi}_x\text{Sb}_{1-x}$ NPs, dried OLA (13 mL) was heated in a 50 mL three neck flask to 160 °C under nitrogen, followed by the injection of $\text{LiN}(\text{iPr})_2$ solution (3.6 mmol, i.e. ~0.38 g, in 2 mL of OLA) and, after 60 s, of SbCl_3 /toluene (0.25 mmol, i.e. ~0.057 g in 0.5 mL toluene). After another 30 s, BiCl_3 (0.25 mmol, i.e. ~0.079 g in 2 mL OLA) was added. The reaction mixture was held for 15 s, following by the same cooling, isolation, and purification procedure as described for In NPs.

Synthesis of Cu_6Sn_5 NPs. In a typical synthesis of 14 nm Cu_6Sn_5 NPs, dried OLA (13 mL) was mixed with CuCl_2 (0.080 g, 0.6 mmol) in a 50 mL three neck flask, additionally dried under vacuum (45 min at 120 °C), and heated to 180 °C under nitrogen, followed by the injection of $\text{LiN}(\text{iPr})_2$ solution (3.6 mmol, i.e. ~0.38 g, in 2 mL of OLA) and, after 30 s, of SnCl_2 (0.5 mmol, ~0.095 g, in 3 mL OLA). The reaction was held for 4 h, followed by the same cooling, isolation, and purification procedure as described for In NPs.

Synthesis of Cu₂Sb NPs. In a typical synthesis of 16 nm Cu₂Sb NPs, dried OLA (13 mL) was mixed with of CuCl₂ (0.134 g, 1 mmol) in a 50 mL three neck flask, additionally dried under vacuum (45 min at 120 °C), and heated to 180 °C under nitrogen, followed by the injection of LiN(SiMe₃)₂ solution (3.6 mmol, i.e., ~0.6 g in 1 mL of toluene) and, after 30 s, of SbCl₃/toluene (0.5 mmol, ~0.114 g in 2 mL toluene). The reaction was held for 4 h, followed by the same cooling, isolation, and purification procedure as described for In NPs.

Synthesis of Zinc NPs. In a typical synthesis of 27 nm Zn NPs, dried OLA (13 mL) was mixed with anhydrous ZnCl₂ (0.068 g, 0.5 mmol), kept under vacuum at 120 °C for 1 h, and heated to 270 °C under nitrogen. LiN(SiMe₃)₂ (3.6 mmol, 0.6 g) dissolved in dried OLA (2 mL) was injected at this temperature. After ca. 30–60 s, the solution color had gradually changed from yellow to dark brown, indicating the formation of Zn NPs. After additional 2 min of growth, the reaction mixture was cooled to room-temperature. The purification and isolation of Zn NPs was carried out in the glovebox using dried toluene and ethanol, followed by redispersion in toluene. Samples for TEM were transferred from the glovebox in airtight bags and only briefly exposed to air during the sample loading into the electron microscope. For obtaining larger NPs, OLA was replaced with ODE, except for using ca. 2 mL of OLA for dissolving LiN(SiMe₃)₂.

Synthesis of Ga NPs. In a typical synthesis of 22 nm Ga NPs, dried ODE (12 mL) and dried DOA (1.13 mL, 3.75 mmol) were added into a 50 mL three neck flask, kept under vacuum for 60 min at 120 °C under constant stirring. The temperature of the ODE/DOA mixture was raised to 250 °C under N₂, followed by the injection of the Bu-Li solution (3.6 mmol, 1.33 mL, 2.7 M in heptane). After around 30 s, GaCl₃ (0.022 g in 0.5 mL of toluene) was injected, inducing the gradual solution color change from yellow to brown, indicating the formation of Ga NPs. After another 30 s, the reaction solution was quickly cooled down to room temperature using air-cooling and a water-ice bath, including injection of toluene (12 mL, at 150 °C). Then, OA (0.2 mL) was added at 50 °C. Ga NPs were precipitated by ethanol (25 mL), followed by centrifugation at 6000 rpm for 4 min. Ga NPs was redispersed in toluene (5 mL) containing OA (0.1 mL) to replace the weakly bound OLA and then again precipitated by ethanol (5 mL) followed by centrifugation at 6000 rpm for 1 min. Finally, Ga NPs were dispersed in toluene.

Characterization. Transmission electron microscopy (TEM) images were obtained with Philips CM30 TEM microscope operated at a voltage of 300 kV. Carbon-coated TEM grids from Ted-Pella were used as substrates. An aberration-corrected HD-2700CS microscope (Hitachi, cold-field emitter, 200 kV) was used for scanning TEM (STEM) investigations. Energy dispersive X-ray (EDX) spectroscopy was performed on Hitachi S-4800 SEM microscope with aluminum as substrate. X-ray diffraction (XRD) patterns were collected on STOE STADI P diffractometer. Solution ¹H, ⁷Li, and ¹¹⁹Sn nuclear magnetic resonance (NMR) spectra were recorded using a Bruker DRX 500 spectrometer. ¹H spectra were obtained at room temperature with locking. The pulse width was set at 10 μs, and the relaxation delay was 1 s. The number of scans used for experiments was 8–100. The NMR samples were prepared in a 5 mm tube in a glovebox using C₆D₆ as solvent. All spectra were referenced to tetramethylsilane. ⁷Li NMR spectra were obtained at room temperature with locking. The pulse width was set at 10–30 μs, and the relaxation delay was 0.5–1 s. The number of scans used for experiments was 128. All ⁷Li NMR spectra were referenced to LiCl (0.5 M in D₂O). ¹¹⁹Sn NMR spectra were recorded at room temperature using a pulse width of 10 μs and the relaxation delay of 0.5 s and referenced to Sn(CH₃)₄.

Computational Methodology. Metal-oleylamides were considered as isolated molecules, whose geometry was optimized at DFT level by using DMOL³ code, as implemented in Materials Studio 6.0. The exchange-correlation functional and the dispersion contribution, as well as the effective core-potential and the basis set were set, was reported elsewhere.²⁶ In addition, the molecular systems were treated as canonical ensembles (NVT) at different temperatures in the molecular dynamics simulations. The core electrons were treated using effective core potentials for In, Sn, and Sb systems, and for Bi all electron relativistic calculations were done. In fact, because of its large atomic number, Z = 83, relativistic effects are to be considered for bismuth, as

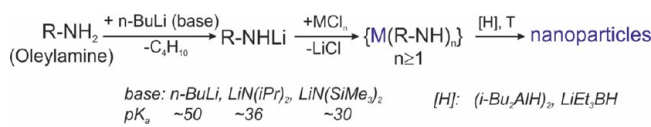
recently discussed.⁶¹ We use the gradient-corrected functional (GGA) of PBE type and double numeric polarized basis set (DNP3.5) for the basis set atomic orbitals, as implemented in DMol³. For OLA and Li-oleylamide we use the triple numeric polarized basis set TNP3.5. The dispersion correction of the form C₆R⁻⁶ are accounted into DFT formalism by using the Grimme scheme⁶² for all systems except Bi(OAm)₃, for which the implementation is not yet available in DMol³ code. The convergence tolerance in the geometry optimization of the energy, maximum atomic force, and maximum atomic displacement are set to 1.0 × 10⁻⁵ Ha, 0.001 Ha/Å and 0.001 Å, respectively.

■ RESULTS AND DISCUSSION

On the in Situ Formation of Metal–Oleylamides. Oleylamine (*cis*-9-octadecenoic amine, *cis*-CH₃(CH₂)₇CH=CH(CH₂)₈NH₂, OLA) is the dominant coordinating solvent in nanomaterials synthesis.^{63–66} Being liquid at room temperature (T_m ~ 20 °C), it boils without decomposition at ~360 °C, providing a broad window for adjusting the reaction temperatures. OLA can coordinate and solubilize both lyophilic metal complexes as well as conventional metal salts such as chlorides. OLA is usually used as received from common chemical vendors, without further purification, and is available in several grades (40–95% in primary amine content). ¹H NMR spectra of OLA from several suppliers (Supporting Information Figure S1) and after vacuum drying at 100 °C indicate [CH₂]:[NH₂] ratios of 13–14 (close to theoretical 15) for “70–95%” OLA (from TCI, Acros, Aldrich) but a higher ratio of 24 for “40%” OLA (from TCI). This higher ratio can be attributed to the presence of high-boiling hydrocarbons, as no other functional groups can be seen in NMR spectra. In the following all results are presented for “40%” OLA from TCI (most inexpensive option), as control experiments with “70%” Aldrich and “95%” TCI products gave undistinguishable results. We note that standard vacuum distillation of OLA does not significantly alter the NMR spectrum.

In a one-pot NP synthesis proposed in this study (Scheme 1), inexpensive metal chlorides are used as metal precursors and

Scheme 1. Outline of the One-Pot Synthesis of Inorganic NPs Using in Situ Formed Metal–Oleylamides (X-type ligation)^a



^aThe formation of metal–oleylamides is promoted by the addition of a strong organic base. Both oleylamine (L-type ligand) and oleylamide (X-type ligand) coordinate the NP surface providing colloidal stability. M = In, Sn, Bi, Sb, Zn, Cu, Ga.

OLA serves as a coordinating solvent and as a source of oleylamido ligands for the in situ formation of metal–amides. OLA can coordinate metal atoms or ions either as a neutral molecule (L-type ligation, e.g. amino-complexes) or, more strongly, as RNH[−] anion (X-type ligation, amido-complexes). For X-type ligation RNH₂—as a very weak acid—has to be deprotonated. We therefore used *n*-BuLi, an inexpensive and strong base commonly used in organic chemistry, which quickly and quantitatively converts RNH₂ into RNHLi, releasing butane (Scheme 1). Note that although *n*-BuLi is flammable and should be handled with care using glovebox and airtight syringes,⁶⁷ it is considerably safer than *tert*-BuLi. Its flammability is also lower when dilute 0.5–1 M solutions in toluene or THF are used. After deprotonation of OLA, metal-oleylamide is then formed by

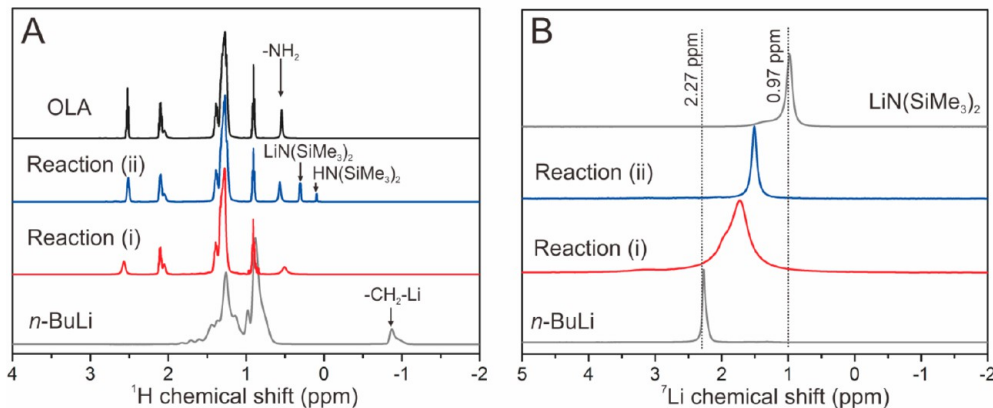


Figure 1. (top) Acid–base reactions between OLA and *n*-BuLi or LiN(SiMe₃)₂. (A) ¹H NMR and (B) ⁷Li NMR spectra after reactions (i) and (ii). Experimental OLA:base ratio was 10:1. Reference spectra of pure *n*-BuLi, OLA, and LiN(SiMe₃)₂ are also presented here and in Supporting Information Figure S2 (¹H spectrum of LiN(SiMe₃)₂). All samples were diluted in C₆D₆. To mimic the actual reaction conditions, reactions were carried out at 150 °C. The degree of LiN(SiMe₃)₂ → RNHLi conversion was estimated from the amount of released HN(SiMe₃)₂. The solvation with OLA molecules is not included into chemical formulas.

methathesis reaction between MCl_n and RNHLi. M–oleylamide species can be stable (Sn, In, no decomposition for at least a minute) or fully unstable (Bi, Sb, Cu), immediately forming NPs. Note that OLA itself is a mild reducing agent. For rather stable amides, the formation of NPs can be induced by injecting organic-soluble reducing agents such as lithium triethylborohydride, Li[Et₃BH] (also known as “super-hydride”), and diisobutylaluminum hydride (DIBAH), (i-Bu₂AlH)₂. A general observation is that, due to steric encumbrance, oleylamides are generally much less stable than homoleptic silyl- or alkylamides.²⁶ Moderate reaction temperatures of 100–200 °C favor the spherical shape for NPs of low melting point metals such as Sn (231 °C), In (157 °C), and Bi (271 °C) or Ga (29.8 °C).

Deprotonation of OLA by *n*-BuLi (reaction (i)) as well as by weaker but safer amide bases such as LiN(SiMe₃)₂ (reaction (ii)) has been carefully followed with ¹H and ⁷Li NMR spectra (Figure 1). The basicity of an organic base (R[−], RNH[−], R₂N[−]) is characterized by the pK_a of a corresponding conjugate acid (R-H, RNH₂, R₂NH). The higher the pK_a, the stronger the proton acceptor. ¹H NMR spectra indicate that *n*-BuLi, being one of the strongest known bases (pK_a ~ 50),⁶⁸ can quickly and fully deprotonate OLA via irreversible reaction (i). A more complex picture is expected and observed for amides as bases. If, for instance, LiN(SiMe₃)₂ is introduced into OLA, at least four different species may coexist in equilibrium—LiN(SiMe₃)₂, oleyl-NH₂, and oleyl-NHLi, HN(SiMe₃)₂ (reaction ii, Figure 1). All amines are derivatives of NH₃ (pK_a = 35), and their pK_a values span a broad range of 26–38 depending on both their molecular structure and the environment.⁶⁹ Further, Brønsted basicity of such long-chain amines as OLA had not been reported so far. In fact, tabulated pK_a values are often of very little predictive power, and it is a combined effect of electronic induction, solvation, sterics, and molecular aggregations that determines selectivity of deprotonation/lithiation in monoalkylamine/dialkylamine mixtures.^{70,71} Nearly all amides exist in oligomeric forms [(R₂NLi)_n] and [(RNHLi)_n], which may also include neutral amine molecules for solvation. The possibility of forming such aggregates or polymers with each Li bridging three anionic centers is the main driving force for primary amine lithiation.

Taking these considerations into account, it is not surprising that a rather weak base LiN(SiMe₃)₂ (pK_a ~ 26–30, in THF)^{69,72} establishes an acid–base equilibrium (ii) with OLA, in which ca. 15% of LiN(SiMe₃)₂ is converted into RNHLi. As will be shown below, this degree of deprotonation by LiN(SiMe₃)₂ is sufficient for promoting fast formation of metal–oleylamido species. Dilakylamides such as lithium diisopropylamide (LiN(iPr)₂, pK_a ~ 36–37)⁶⁹ show a behavior intermediate between LiN(SiMe₃)₂ and *n*-BuLi.

LiN(SiMe₃)₂ in noncoordinating solvents such as C₆D₆ forms dimers or tetramers^{73–75} ($\delta(^1\text{H})$ = 0.13 ppm, Supporting Information Figure S2), whereas with large coordinating molecule such as OLA a presumably monomeric solvate LiN(SiMe₃)₂OLA is observed with $\delta(^1\text{H})$ = 0.31 ppm for –SiMe₃ protons (Figure 1). Corresponding ⁷Li NMR spectra (Figure 1B) are also considerably different for noncoordinating solvent (C₆D₆) and in the presence of OLA. In reaction (ii) most of the Li-ions exist as a solvate LiN(SiMe₃)₂OLA, whereas RNHLi with certain degree of solvation and aggregation^{74,76} dominates the *n*-BuLi-based reaction (BuLi:OLA = 1:10). When excess of *n*-BuLi is applied (BuLi:OLA molar ratio of 1.25–3), an *N,N*-dilithiooleylamine (RNLi₂) is formed and all NH₂ protons disappear in NMR spectra (Supporting Information Figure S3).

NMR observation of in situ formed metal amides was conducted for Sn and In, which form sufficiently stable amides with both silylamine and oleylamido ligands. While the *n*-BuLi-based approach is simple and offers purely oleylamido-ligation, there are two ligands available in LiN(SiMe₃)₂/OLA solution due to acid–base equilibrium (ii, Figure 1). ¹H NMR spectra for stoichiometric reactant ratio reveal complete consumption of LiN(SiMe₃)₂, indicating that Sn²⁺ preferentially binds to RNH[−] fully shifting the equilibrium to the (ii) right-hand side. ¹¹⁹Sn NMR spectra of SnCl₂/LiN(SiMe₃)₂/OLA are identical to those of SnCl₂/*n*-BuLi/OLA solutions (Figure 2C) and show only one peak at 62.5 ppm fully confirming the formation of only Sn–oleylamide in both cases. Controls show ¹¹⁹Sn chemical shifts for Sn[N(SiMe₃)₂]₂ and SnCl₂ in OLA at 646 ppm and −420 ppm, respectively.

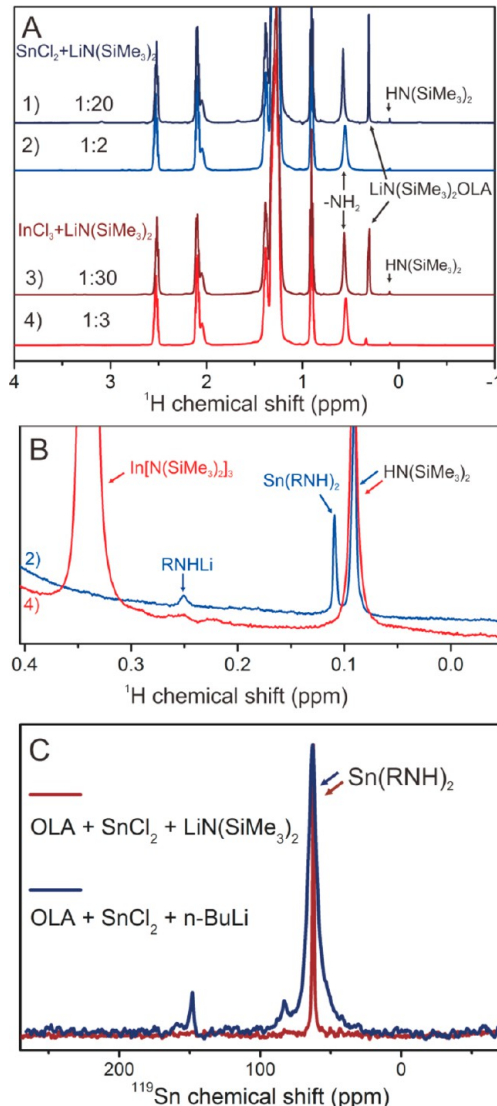


Figure 2. (A, B) ^1H NMR for $\text{SnCl}_2\text{-LiN}(\text{SiMe}_3)_2$ and $\text{InCl}_3\text{-LiN}(\text{SiMe}_3)_2$ solutions in OLA (reacted at 150 °C, diluted in C_6D_6). Stoichiometric metal-to-LiN($\text{SiMe}_3)_2$ ratios as well as 10-fold excess of LiN($\text{SiMe}_3)_2$ were compared. (C) ^{119}Sn NMR spectra of Sn-oleylamide formed by the action of either LiN($\text{SiMe}_3)_2$ or $n\text{-BuLi}$.

A different scenario is observed for In. At stoichiometric ratios of InCl₃ and LiN($\text{SiMe}_3)_2$ (i.e., 1:3), ca. ~20% of In is converted into In[N($\text{SiMe}_3)_2]_3$. This seemingly subtle difference between Sn and In has a drastic effect on the NP formation, exemplifying the importance of mechanistic studies. At this stoichiometric InCl₃-to-LiN($\text{SiMe}_3)_2$ ratio, a bimodal mixture of large (50–100 nm) and small (~10 nm) In NPs can be observed (Supporting Information Figure S4A). We assume that larger NPs form from In[N($\text{SiMe}_3)_2]_3$, because a very similar outcome of the reaction is observed by replacing OLA with trioctylphosphine (TOP), in which only In[N($\text{SiMe}_3)_2]_3$ can be formed *in situ* (Supporting Information Figure S4B). Small NPs originate from the reduction of In-oleylamide. The formation of In[N($\text{SiMe}_3)_2]_3$ is fully suppressed only for the large 10-fold excess of LiN($\text{SiMe}_3)_2$, because of the larger amount of RNHLi formed.

Insight from DFT and Molecular Dynamics Simulations. As a first step, the geometries of isolated molecules of metal-oleylamides were optimized at DFT-D level of theory to get the equilibrium bond lengths and the total energies at $T = 0$ K.

K. The binding energy (E_b , Table 1) of the M–N bonds were calculated as the mean value of all M–N bonds in the molecule.

Table 1. Bond Lengths (M–N, in Å) and Binding Energies (E_b , in kJ/mol) of the Metal–Nitrogen Bonds in Corresponding Oleylamides, Calculated at DFT-D Level of Theory by Using DMol3 Code at $T = 0$ K^a

M	E_b	$d(\text{M-N})$	$d(\text{M-N})$	M–N coordination
H	551.66	1.022		H–N–H angle 105.97°
Li	310.83	1.735		Li–N–H angle 124.09°
In	233.81	2.153	2.127	trigonal planar
Sn	337.69	2.087	2.086	N–Sn–N angle 91.55°
Sb	314.25	2.084	2.095	trigonal pyramid
Bi	38.11 (77.81)	2.248	2.249	trigonal pyramid

^aFor comparison, we report the same calculations for M = H.

Interestingly, for Bi(RNH)₃, treating the Bi core region explicitly (all electrons) and including the relativistic effects make the total energy convergent much better without the typical oscillation we found when the core electrons are treated via an effective core potential. In addition, as expected, the binding energy of Bi–N bonds decreases by almost 50% of the nonrelativistic potential of Bi atom (see the value in brackets, Table 1). The Bi–N energy is almost 10 times smaller than for other studied molecules. Another common trend is that M–N bond energies in oleylamides are considerably smaller than in silylamides (our earlier study, see ref 26). The (M–N) thermal behavior of isolated M–oleylamide molecules was assessed via molecular dynamics simulations of isolated molecules, considered as NVT ensemble. In agreement with the experiment, all studied molecules do not undergo thermal decomposition at $T = 100$ °C, except Bi–oleylamide in which one of the amido ligands detaches due to homolysis of the Bi–N bond (see comparison of In and Bi in Figure 3).

In Bi–oleylamide, the Bi–N bonds are thermally activated before any C–H bond cleavage. The latter is the leading process of the thermal decomposition of all other M–oleylamides at temperatures above 200 °C. A large elongation of Sb–N bonds of about 8% is observed at $T = 200$ °C, again in good agreement with reduced stability of this amide. We have not considered Cu and Zn as their amides are not expected to be monomeric, but rather polynuclear, as discussed by M. F. Lappert et al.³⁵

Synthesis of In and Sn NPs: The Case of Stable Amides.

In agreement with the role of In–oleylamide as precursor, size-tunability in the range of 7–22 nm with the excellent size distributions not exceeding 5% were obtained for both bases—LiN($\text{SiMe}_3)_2$ and $n\text{-BuLi}$ (Figure 4, synthesis details in Supporting Information Table S1). For both bases, we obtained very similar trends in the evolution of the mean In NPs size upon adjustment of the concentrations of InCl₃ and superhydride or by varying the reaction time (Supporting Information Tables S7–S12). In particular, higher concentration or longer reaction time lead to expected increases of NPs size, whereas higher amount of reducing agent decreases the size, presumably due to higher nucleating rate producing more nuclei and thus reducing the amount of precursor stock available for growing each NP. Since the reaction temperature (150–160 °C) is very close to the melting point of bulk In (156.6 °C), the NPs are assumed to stay in liquid form during nucleation and growing, minimizing the

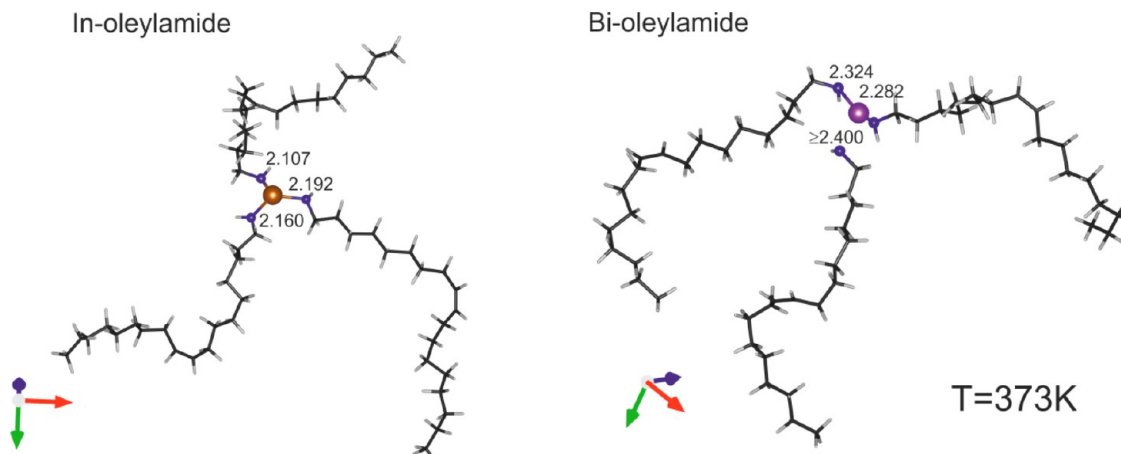


Figure 3. Two snapshots of the molecular dynamics of In and Bi oleylamides at $T = 100\text{ }^{\circ}\text{C}$ (373 K), along with In–N and Bi–N bond distances (in Å).

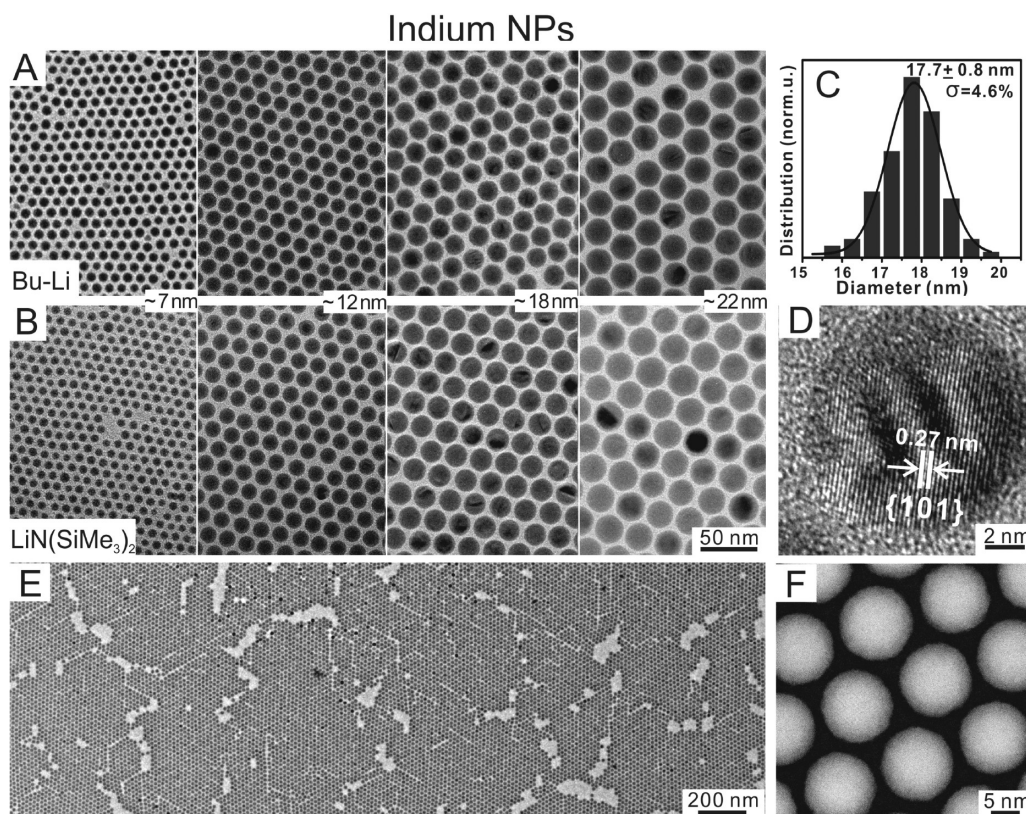


Figure 4. TEM images of In NPs. (A) and (B) illustrate that the same size tuning range of 7–22 nm can be obtained with $n\text{-BuLi}$ and $\text{LiN}(\text{SiMe}_3)_2$ bases. (C) Size histogram for 18 nm In NPs ($n\text{-BuLi}$ based); (D) HRTEM image of a single In NP. (E) Low-magnification TEM image of 12 nm In NPs ($n\text{-BuLi}$ based) illustrating high uniformity of In NPs, along with (F) HAADF-STEM image. Synthesis details for each sample are provided in Supporting Information Table S1.

surface energy in the molten state giving (nearly) perfectly spherical shape of In NPs. Detailed structural and compositional characterization using XRD (Supporting Information Figure S5, with Rietveld refinement for 20 nm In NPs), selected-area electron diffraction (SEAD, Supporting Information Figure S5), and energy dispersive X-ray spectroscopy (EDX, Supporting Information Figure S6) confirm the formation of highly crystalline and chemically pure tetragonal In NPs (space group No. 138, $I4/mmm$, $a = b = 0.325$, $c = 0.494$ nm, JCPDF no. 050642). Indium NPs fully crystallize upon cooling to room-temperature with the mean Scherrer size identical to the one estimated from TEM. In comparison with previous synthetic

routes, where organometallic and coordination precursors such as $[\text{In}(\text{h}-\text{C}_5\text{H}_5)]^{77}$ or $\text{In}(\text{N}(\text{SiMe}_3)_2)_3^{45}$ were utilized, our method is based on readily commercially available, low-cost precursors.

In full analogy to In, also Sn NPs can be obtained using $n\text{-BuLi}$ as a base (Figure 5), with the reaction time as a main parameter for tuning the mean particle size. The time evolution of the size distribution monitored over the period of 30 s to 6 h (Supporting Information Table S13) shows clear size-focusing until 1.5 h (size distribution of 4–5%) and defocusing afterward (size distribution of 15% after 6 h). The focusing regime can be attributed to the diffusion-controlled growth under high oversaturation by

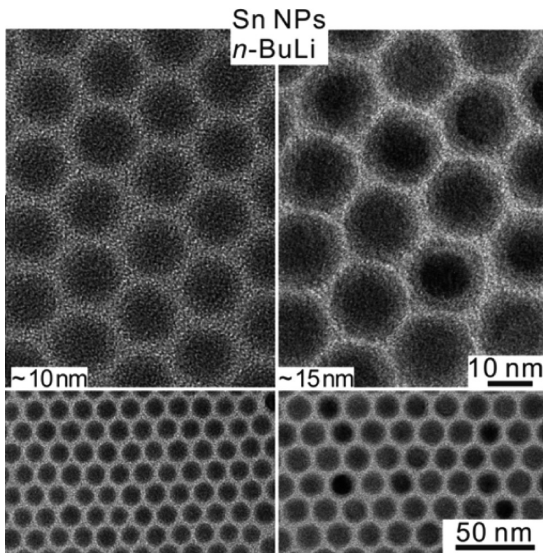


Figure 5. TEM images of Sn NPs obtained using *n*-BuLi as reaction promoter. Detailed information for each sample is provided in Supporting Information Table S13.

monomers, whereas defocusing can be attributed to Ostwald ripening at depletion of the monomer concentration.⁷⁸ The XRD pattern with Rietveld refinement and SAED (Supporting Information Figure S7) can be indexed to tetragonal Sn (known as β -Sn, space group No. 141, $I41/amd$, $a = b = 0.583$, $c = 0.318$ nm, JCPDF no. 040673). Upon exposure to air, Sn NPs are covered with the amorphous layer of SnO_2 , as confirmed by solid-state ^{119}Sn NMR spectra (Supporting Information Figure S8) and high-resolution HAADF-STEM and bright-field STEM images (Supporting Information Figure S9).

Case of Unstable Amides: Synthesis of Bi, Sb, Cu, and Zn NPs. Synthesis of Bi NPs illustrates the high utility of unstable amides, which decompose without addition of reducing agents. Similarly to In NPs, both bases—*n*-BuLi and $\text{LiN}(\text{SiMe}_3)_2$ —provide high monodispersity and size-tuning range of 10–21 nm (Figure 6). In $\text{LiN}(\text{SiMe}_3)_2$ -based synthesis, size adjustment can be most conveniently accomplished by varying the reaction temperature in the 90–150 °C range, while keeping very short reaction time of ~10 s (after injection of $\text{LiN}(\text{SiMe}_3)_2$, see details in Supporting Information Table S2). In *n*-BuLi based synthesis, the same size-tuning range can be achieved only through the combined effect of the growth temperature and reaction time (Supporting Information Tables S2 and S14). HR-TEM images

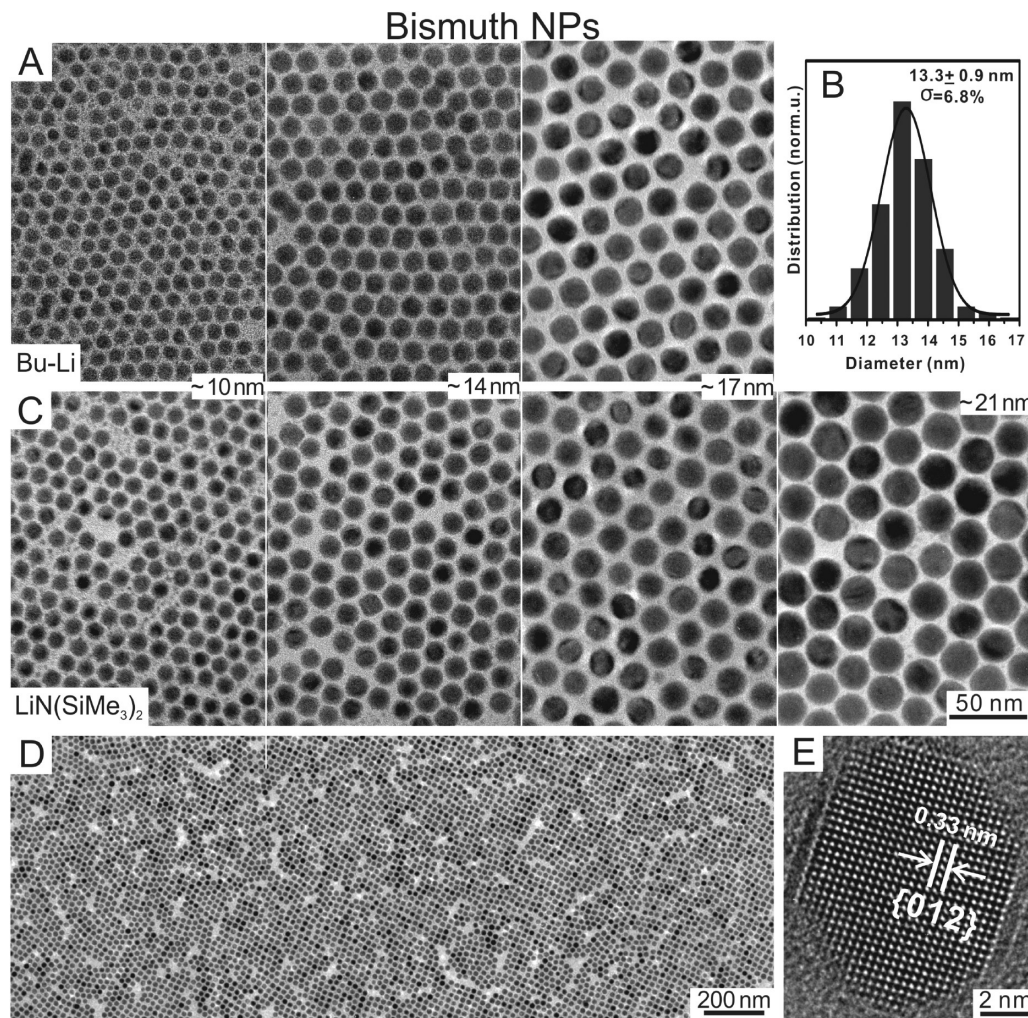


Figure 6. TEM images of Bi NPs. (A) and (C) illustrate that the same size tuning range of 10–21 nm ca. be obtained with *n*-BuLi and $\text{LiN}(\text{SiMe}_3)_2$ bases. (B) Size histogram for 13 nm Bi NPs (*n*-BuLi based). (D) Low-magnification TEM image of from 13 nm sample (*n*-BuLi based). (E) HRTEM of a single Bi NP. Synthesis details for each sample are provided in Supporting Information Table S2.

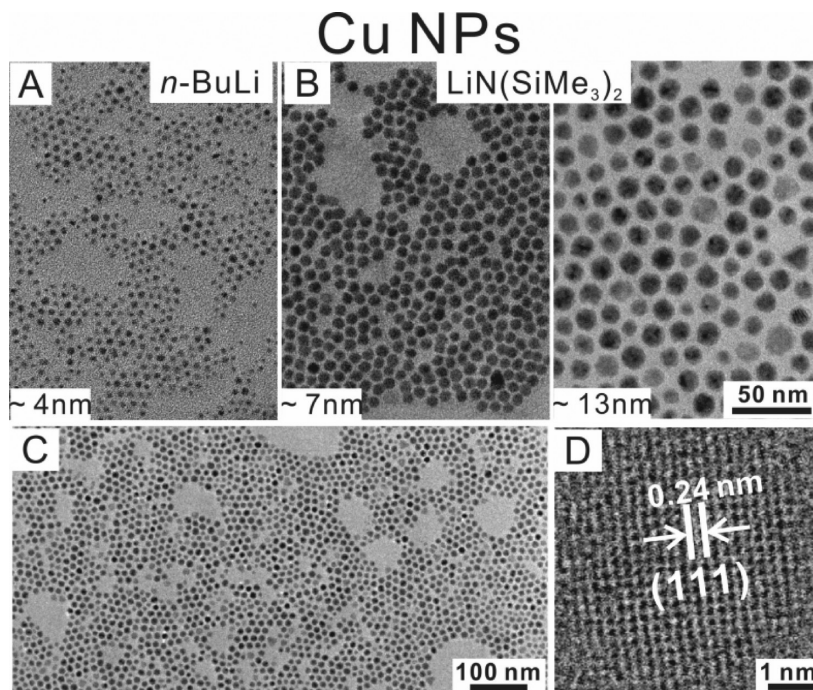


Figure 7. TEM images of 4, 7, and 13 nm Cu NCs from (A) *n*-BuLi based and (B) LiN(SiMe₃)₂ based synthesis, (C) low-resolution TEM image of the 13 nm sample, and (D) HRTEM image of a single Cu NP. Detailed information for each sample is provided in Supporting Information Table S4.

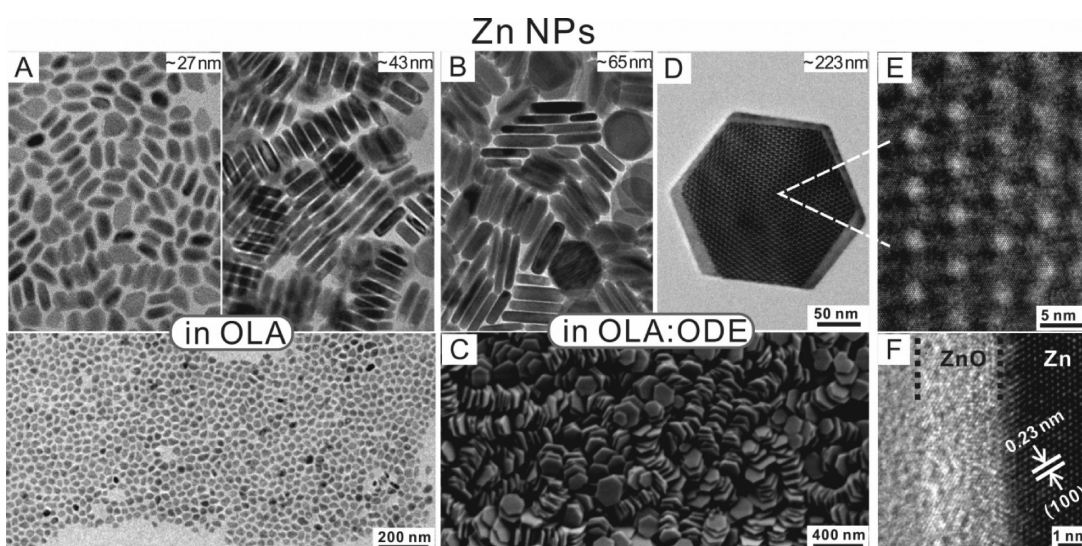


Figure 8. (A, B, D, E, F) TEM and SEM (C) images of Zn NPs obtained via LiN(SiMe₃)₂-based approach. The mean size is adjusted in the 20–220 nm range by the growth temperature and by diluting OLA with ODE (large sizes). (A) Examples of 27 and 43 nm Zn NPs, with lower panel showing low-resolution image of 27 nm sample. (B, D, E) Examples of ~65 nm and ~220 nm Zn NPs along with (C) SEM image of ~220 nm sample. (D, E) Illustrations of Moire fringes formed by stacking two platelet-shaped Zn NPs. (F) High-resolution image from the edge of Zn NP showing ZnO shell formed immediately upon exposure to air. Detailed information for each sample is provided in Supporting Information Table S5.

(Figure 6E), XRD patterns (for 11 and 20 nm, with Rietveld refinement, Supporting Information Figure S5), SAED (Supporting Information Figure S5), and EDX pattern (Supporting Information Figure S6) have confirmed the formation of highly crystalline, rhombohedral Bi (space group No. 166, $R\bar{3}m$, $a = b = 0.455$, $c = 1.186$ nm, JCPDF no. 441246).

Nearly spherical shape can be again attributed to the low melting point of Bi, which leads to either nucleation in the liquid form (due to size-dependence of the melting) or enhanced surface diffusion/surface melting during the growth. Analogously to Bi, also the 11–19 nm Sb NPs can be synthesized using *n*-BuLi

base (Supporting Information Table S15). Sb NPs have a crystal structure of rhombohedral Sb (space group No. 166, $R\bar{3}m$, $a = b = 0.431$, $c = 1.127$ nm, JCPDF no. 350732), as illustrated with XRD patterns (Supporting Information Figure S7).

The proposed one-pot, oleylamide-based synthesis of inorganic NPs can be readily extended also to transition metals, including those of very different electronegativity such as seminoble 4–14 nm Cu NPs (Figure 7, Supporting Information Table S19) and 20–200 nm Zn NPs (Figure 8). Both metals readily form in zero-oxidation state without reducing agents, pointing to the highly favorable effect of instability of the

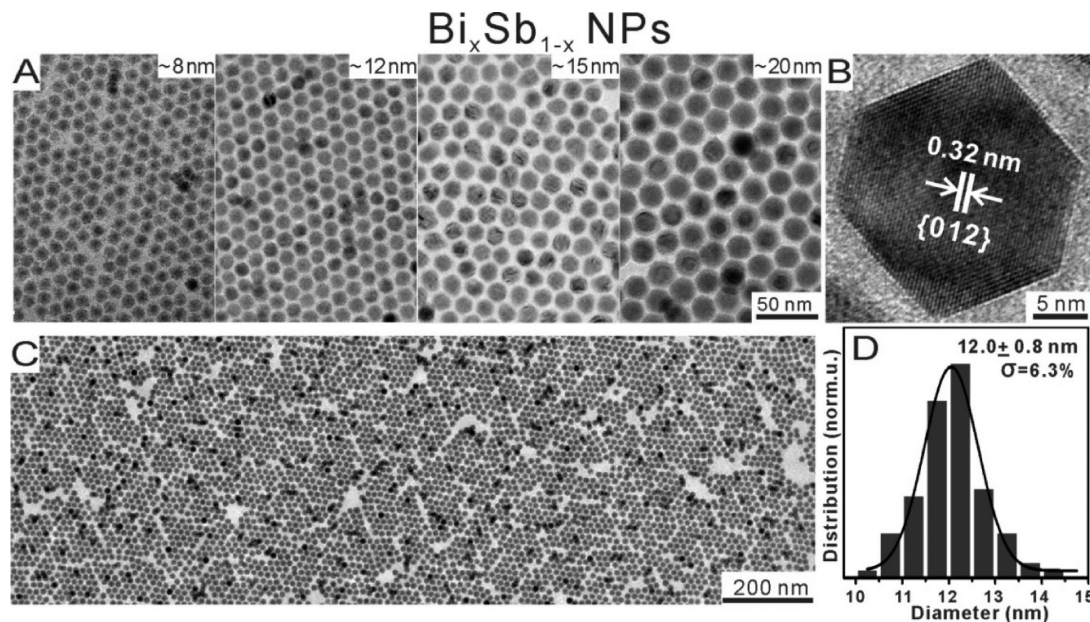


Figure 9. (A) TEM images of 8–20 nm $\text{Bi}_x\text{Sb}_{1-x}$ NPs; (B) HRTEM of a single $\text{Bi}_x\text{Sb}_{1-x}$ NP; (C) low resolution TEM image; and (D) size-histogram for 12 nm sample. Detailed information for each sample is provided in Supporting Information Table S3.

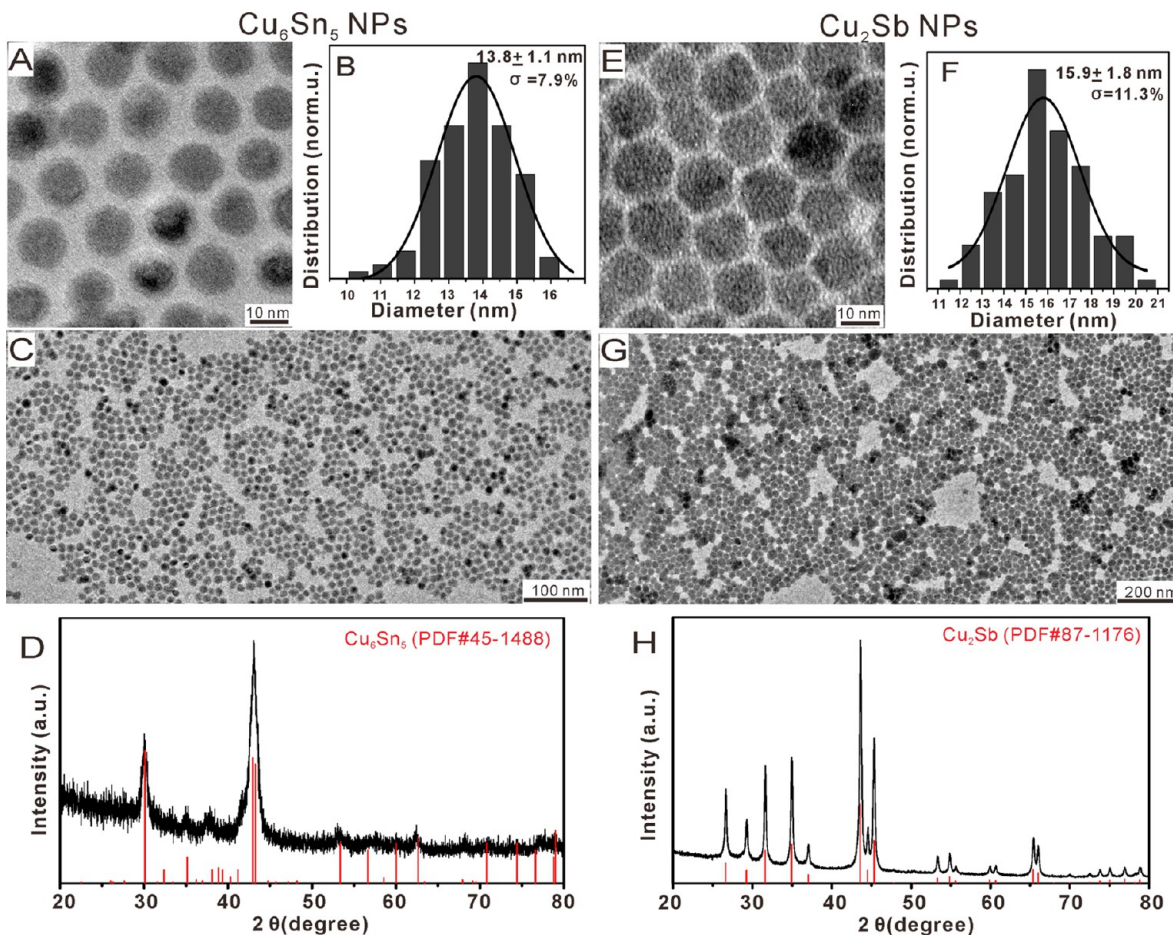


Figure 10. (A, C) TEM images, (B) size histograms of 14 nm sample, and (D) XRD pattern of Cu₆Sn₅ NPs. (E, G) TEM images, (F) size histograms of 16 nm sample, and (H) XRD pattern of Cu₂Sb NPs.

intermediate bulky metal oleylamides. We note that this is the first example of highly uniform Zn NPs. Two previous reports have yielded highly polydisperse, irregularly shaped NPs.^{79,80}

Our preliminary results also indicate that an analogous synthetic procedure is also applicable to a great variety of transition metals such as Fe, Co, Ni, etc.

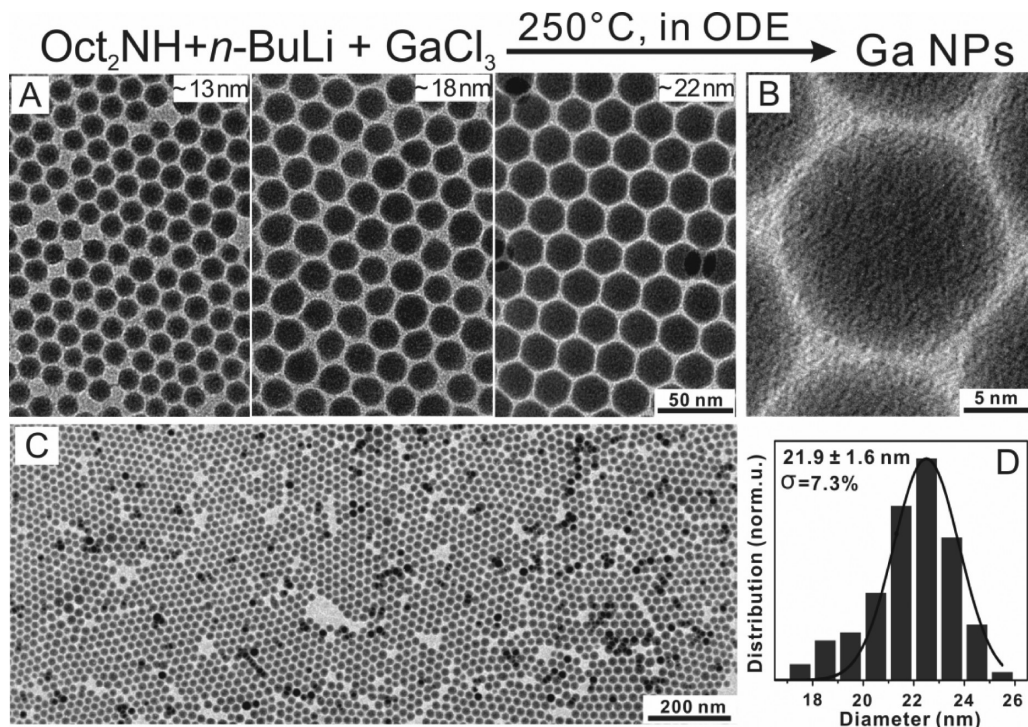


Figure 11. (A) TEM images of 13–22 nm Ga NPs synthesized using DOA, with *n*-BuLi as proton abstractor. (B) High-resolution TEM image illustrating the lack of crystallinity at ambient conditions and (C) corresponding low-resolution image and (D) size histograms of 22 nm sample. Detailed information for each sample is provided in Supporting Information Table S6.

The smallest Cu NPs of ~ 4 nm mean size were obtained in *n*-BuLi based synthesis, whereas larger 7–14 nm Cu NPs were obtained via $\text{LiN}(\text{SiMe}_3)_2$ approach by adjusting the reaction temperature and CuCl_2 concentration (Supporting Information Table S19). Cu NPs are of high interest due to their catalytic properties, such as in the electrochemical methanation of CO_2 ,⁸¹ as well as due to their plasmonic properties and high electrical conductivity. So far, there have been only very few reports on highly uniform Cu NPs, such as ~ 50 –200 nm nanocubes,^{82,83} nanowires,^{83,84} and 8–14 nm spherical Cu NPs.⁸⁵ The synthesis proposed here not only is simple but also features a fully oxygen-free environment that prevents the formation of oxide impurity. Yet the Cu_2O does form upon exposure of Cu NPs to air as can be seen from XRD patterns (Supporting Information Figure S5) as well as from the electron diffraction patterns (Supporting Information Figure S5).

In the synthesis of Zn NPs using $\text{LiN}(\text{SiMe}_3)_2$ as a base, we have tested one other approach for controlling the reaction kinetics—dilution of the OLA with noncoordinating solvent such as octadecene (ODE). For example, for the synthesis of large Zn NPs (Figure 8B,D), OLA was used only to dissolve $\text{LiN}(\text{SiMe}_3)_2$, and this solution was injected into ZnCl_2 /ODE solution. Hence the amount of OLA was reduced sevenfold. All Zn NPs are highly crystalline and just like bulk Zn adopt hexagonal close packed lattice (see XRD pattern in Supporting Information Figure S11). The largest Zn NPs adopt a hexagonal shape and are generally too large for high-resolution imaging of their crystal lattice. Yet many of these hexagons tend to form vertical stacks. Two hexagons are nearly ideal for observing rotational Moiré patterns, formed by two overlapping patterns (Figure 8D,E and Supporting Information Figure S12). The spacing between Moiré fringes (d_m) of these nanoplates along the [001] viewing direction is determined by the rotation angle around the {100} direction, as illustrated in Supporting

Information Figure S12. For example, the rotation angle between two hexagons in Figure 8D is 4.2, yielding a d_m of 3.1 nm.

Examples of Binary Alloy NPs: $\text{Bi}_{1-x}\text{Sb}_x$, Cu_6Sn_5 , and Cu_2Sb . The proposed shortcut synthesis using *in situ* formed long-chain alkylamides can be extended to alloys and compounds, as exemplarily shown here for $\text{Bi}_x\text{Sb}_{1-x}$, Cu_6Sn_5 , and Cu_2Sb . Binary 8–20 nm $\text{Bi}_x\text{Sb}_{1-x}$ alloy NPs (Figure 9, Supporting Information Table S3) with narrow size distributions (5–10%) were produced via successive reduction of corresponding Bi and Sb chlorides. Such NPs can be of high interest for low-temperature thermoelectric devices.⁴⁹ In a typical successive reduction synthesis, less-reactive precursor (SbCl_3) is first reduced to generate the seeds, followed by the injection of a second chloride (BiCl_3) in 10–30 s intervals. The particle size can be conveniently tuned by the precursor concentration (Supporting Information Table S16), growth temperature (Supporting Information Table S17), or reaction time (Supporting Information Table S18). The compositional tunability can be illustrated for 15 nm $\text{Bi}_{0.8}\text{Sb}_{0.2}$ NPs using XRD pattern (Supporting Information Figure S10), in which reflection peaks are shifted to higher 2θ angles due to reduction of the lattice constant by 1.07% with respect to rhombohedral Bi (corresponding to 20% Sb based on Vegard's law). $\text{Bi}_{0.8}\text{Sb}_{0.2}$ NPs are considerably more faceted than pure Bi NPs. Similar to the synthesis of $\text{Bi}_{1-x}\text{Sb}_x$, a successive reduction method can also be used to synthesize Cu_6Sn_5 alloy (Figure 10a–d) and Cu_2Sb intermetallic compound (Figure 10e–h), and both of them are of high interest as anode material for Li-ion or Na-ion batteries.^{86–89}

Extension to Secondary Amines: Synthesis of Ga NPs via Diocetylamine (DOA). Long-chain secondary amines may also be used as a source of amide ligands for NP synthesis. Analogously to the OLA case discussed above, *n*-BuLi can be quantitatively converted into a secondary amide of Li. Figure 11

illustrates this chemistry applied for a one-pot synthesis of monodisperse 13–22 nm Ga NPs, using DOA as a secondary amine. This example highlights indispensability of secondary amines when primary amines fail to yield reactive interim amide. In fact, our initial attempt to obtain Ga NPs using OLA did not yield Ga NPs due to very low reactivity of Ga–oleylamide, in good agreement with earlier observations of high thermal stability of Ga complexes with bulky primary amines.⁹⁰ Reduced reactivity of primary amides can be related to their ability and tendency to oligomerization forming polynuclear amido- or even imido-complexes.³⁵ This DOA synthesis provides a much simpler alternative to the recently published method relying on presynthesized dimeric tris(dimethylamido)gallium, $\text{Ga}_2(\text{NMe}_2)_6$.⁴⁴ Importantly, in the present study and in ref 44 short growth times of ≤ 30 s were found to be most essential for obtaining monodisperse Ga NPs. Longer growth leads to very fast coalescence of liquid Ga NPs, leading to very broad size distributions (Supporting Information Table S20). All synthesized Ga NPs are noncrystalline, presumably liquid at ambient conditions due to low bulk boiling point of just 29.8 °C and well-known tendency to supercooling effect (with $\Delta T/T_m$ as high as 0.5).^{44,91,92}

The noncrystalline nature of Ga NPs can be seen already from conventional high-resolution TEM images (Figure 11B) and from the diffuse rings in the electron diffraction patterns (Supporting Information Figure S13), as well as from the low-resolution TEM images of NP ensembles (Figures 11C) showing highly uniform NP-to-substrate contrast, whereas any noticeable crystallinity of NPs would make some NP darker due to orientation-dependent diffractional contrast. Liquid Ga NPs may become uniquely suitable as low-melting-point catalyst for solution–liquid–solid growth of nanowires,⁹³ in liquid-metal based plasmonics and phase-change devices^{94–98} and as self-healing anode material for Li-ion batteries.⁴⁴

CONCLUSIONS

We report a facile, one-pot synthesis of highly monodisperse NPs (5–30 nm, 5–10% standard size distribution) of various metals and metalloids such as In, Sn, Bi, Sb, Ga, Cu, and Zn, and their alloys $\text{Bi}_{1-x}\text{Sb}_x$, Cu_6Sn_3 , and Cu_2Sb , that relies on the formation of transient highly reactive metal long-chain amides. All syntheses utilize only inexpensive commercial precursors. The proposed reaction mechanism was elucidated and confirmed with multinuclear (^1H , ^7Li , ^{119}Sn) NMR spectroscopy. Metal chloride is first reacted with oleylamine in the presence of strong Brønsted base, such as *n*-butyllithium, that deprotonates oleylamine and thus promotes the formation of metal–oleylamide. We also find that secondary Li-amides such as $\text{LiN}(\text{SiMe}_3)_2$, LiNMe_2 , and $\text{LiN}(\text{iPr})_2$ in place of *n*-butyllithium can be also engaged into Brønsted acid–base equilibria with oleylamine, promoting the formation of metal–oleylamides. Metal–oleylamide is then reduced or thermally decomposed into corresponding metal NPs. This simple methodology allows elimination of elaborate preparation of reactive molecular precursors of these elements, while providing compelling quality of nanomaterials. When *in situ* formed oleylamine is not sufficiently reactive, as in the case of Ga, an *in situ* formed secondary amide precursor (Ga(III)–dioctylamide) can be successfully utilized. Further, this methodology will enable access to previously unknown nanomaterials, as illustrated here by the first synthesis of uniform metallic Zn nanoparticles.

There is a considerable analogy to the modern organic chemistry, with its main trends toward stereoselectivity, atomic

economy, green chemicals, scalability, and increasingly complex molecules. Similarly, we show that through the atomistic understanding of the precursor-to-NC reaction pathway (via mechanistic experimental study and quantum-chemistry simulations), a general chemical strategy with high atomic economy and facile experimental design can be realized. *In situ* generation of the actual highly reactive precursor that precedes the formation of the NCs is of fundamental and practical importance to any NC synthesis, being analogous to the transition state during the formation of molecules in molecular chemistry.

ASSOCIATED CONTENT

S Supporting Information

Experimental details for all syntheses summarized in tables, TEM images, XRD, SAED, EDX patterns, Rietveld refinement, ^1H NMR, and ^7Li NMR spectra are provided. This material is available free of charge via the Internet at <http://pubs.acs.org>.

AUTHOR INFORMATION

Corresponding Author

*E-mail: mvkovalenko@ethz.ch.

Author Contributions

The manuscript was written through contributions of all authors. All authors have given approval to the final version of the manuscript.

Notes

The authors declare no competing financial interest.

ACKNOWLEDGMENTS

This work was financially supported by the Swiss National Science Foundation (SNF, Project 200021_140245) and ETH Zürich. Electron microscopy was performed at ETH Zürich Electron Microscopy Center and EMPA Electron Microscopy Center. We thank Dr. Maryna Bodnarchuk for TEM images of Sb and Zn nanoparticles. The computational software and hardware resources of ETH Zurich are highly appreciated.

REFERENCES

- (1) Talapin, D. V.; Lee, J.-S.; Kovalenko, M. V.; Shevchenko, E. V. *Chem. Rev.* **2009**, *110*, 389–458.
- (2) Yin, Y.; Alivisatos, A. P. *Nature* **2005**, *437*, 664–670.
- (3) Cho, K. S.; Talapin, D. V.; Gaschler, W.; Murray, C. B. *J. Am. Chem. Soc.* **2005**, *127*, 7140–7147.
- (4) Talapin, D. V.; Nelson, J. H.; Shevchenko, E. V.; Aloni, S.; Sadler, B.; Alivisatos, A. P. *Nano Lett.* **2007**, *7*, 2951–2959.
- (5) Milliron, D. J.; Hughes, S. M.; Cui, Y.; Manna, L.; Li, J.; Wang, L.-W.; Alivisatos, A. P. *Nature* **2004**, *430*, 190–195.
- (6) Zeng, H.; Sun, S. *Adv. Funct. Mater.* **2008**, *18*, 391–400.
- (7) Murray, C. B.; Norris, D. J.; Bawendi, M. G. *J. Am. Chem. Soc.* **1993**, *115*, 8706–8715.
- (8) Shevchenko, E. V.; Bodnarchuk, M. I.; Kovalenko, M. V.; Talapin, D. V.; Smith, R. K.; Aloni, S.; Heiss, W.; Alivisatos, A. P. *Adv. Mater.* **2008**, *20*, 4323–4329.
- (9) Carbone, L.; Nobile, C.; De Giorgi, M.; Sala, F. D.; Morello, G.; Pompa, P.; Hytch, M.; Snoeck, E.; Fiore, A.; Franchini, I. R.; Nadasan, M.; Silvestre, A. F.; Chiodo, L.; Kudera, S.; Cingolani, R.; Krahne, R.; Manna, L. *Nano Lett.* **2007**, *7*, 2942–2950.
- (10) Cozzoli, P. D.; Pellegrino, T.; Manna, L. *Chem. Soc. Rev.* **2006**, *35*, 1195–1208.
- (11) Hines, M. A.; Guyot-Sionnest, P. *J. Phys. Chem.* **1996**, *100*, 468–471.
- (12) Kramer, I. J.; Sargent, E. H. *Chem. Rev.* **2013**, *114*, 863–882.
- (13) Anikeeva, P. O.; Halpert, J. E.; Bawendi, M. G.; Bulović, V. *Nano Lett.* **2007**, *7*, 2196–2200.

- (14) Keuleyan, S.; Lhuillier, E.; Brajuskovic, V.; Guyot-Sionnest, P. *Nat. Photonics* **2011**, *5*, 489–493.
- (15) Clifford, J. P.; Konstantatos, G.; Johnston, K. W.; Hoogland, S.; Levina, L.; Sargent, E. H. *Nat. Nanotechnol.* **2009**, *4*, 40–44.
- (16) Jong-Soo, L.; Kovalenko, M. V.; Jing, H.; Dae Sung, C.; Talapin, D. V. *Nat. Nanotechnol.* **2011**, *6*, 348–352.
- (17) Ibanez, M.; Cadavid, D.; Zamani, R.; Garcia-Castello, N.; Izquierdo-Roca, V.; Li, W. H.; Fairbrother, A.; Prades, J. D.; Shavel, A.; Arbiol, J.; Perez-Rodriguez, A.; Morante, J. R.; Cabot, A. *Chem. Mater.* **2012**, *24*, 562–570.
- (18) Kovalenko, M. V.; Spokoyny, B.; Lee, J. S.; Scheele, M.; Weber, A.; Perera, S.; Landry, D.; Talapin, D. V. *J. Am. Chem. Soc.* **2010**, *132*, 6686–6695.
- (19) Choi, J. H.; Fafarman, A. T.; Oh, S. J.; Ko, D. K.; Kim, D. K.; Diroll, B. T.; Muramoto, S.; Gillen, J. G.; Murray, C. B.; Kagan, C. R. *Nano Lett.* **2012**, *12*, 2631–2638.
- (20) Kim, D. K.; Lai, Y. M.; Diroll, B. T.; Murray, C. B.; Kagan, C. R. *Nat. Commun.* **2012**, *3*, 1216.
- (21) Koh, W. K.; Saudari, S. R.; Fafarman, A. T.; Kagan, C. R.; Murray, C. B. *Nano Lett.* **2011**, *11*, 4764–4767.
- (22) Oh, M. H.; Yu, T.; Yu, S.-H.; Lim, B.; Ko, K.-T.; Willinger, M.-G.; Seo, D.-H.; Kim, B. H.; Cho, M. G.; Park, J.-H.; Kang, K.; Sung, Y.-E.; Pinna, N.; Hyeon, T. *Science* **2013**, *340*, 964–968.
- (23) Bodnarchuk, M. I.; Kravchyk, K. V.; Krumeich, F.; Wang, S.; Kovalenko, M. V. *ACS Nano* **2014**, *8*, 2360–2368.
- (24) He, M.; Kravchyk, K. V.; Walter, M.; Kovalenko, M. V. *Nano Lett.* **2014**, *14*, 1255–1262.
- (25) Kravchyk, K.; Protesescu, L.; Bodnarchuk, M. I.; Krumeich, F.; Yarema, M.; Walter, M.; Guntlin, C.; Kovalenko, M. V. *J. Am. Chem. Soc.* **2013**, *135*, 4199–4202.
- (26) Yarema, M.; Caputo, R.; Kovalenko, M. V. *Nanoscale* **2013**, *5*, 8398–8410.
- (27) Mahler, B.; Spinicelli, P.; Buil, S.; Quelin, X.; Hermier, J.-P.; Dubertret, B. *Nat. Mater.* **2008**, *7*, 659–664.
- (28) Hines, M. A.; Scholes, G. D. *Adv. Mater.* **2003**, *15*, 1844–1849.
- (29) Bodnarchuk, M. I.; Kovalenko, M. V.; Groiss, H.; Resel, R.; Reissner, M.; Hesser, G.; Lechner, R. T.; Steiner, W.; Schäffler, F.; Heiss, W. *Small* **2009**, *5*, 2247–2252.
- (30) Puntes, V. F.; Krishnan, K. M.; Alivisatos, A. P. *Science* **2001**, *291*, 2115–2117.
- (31) Sun, S.; Murray, C. B.; Weller, D.; Folks, L.; Moser, A. *Science* **2000**, *287*, 1989–1992.
- (32) Talapin, D. V.; Rogach, A. L.; Kornowski, A.; Haase, M.; Weller, H. *Nano Lett.* **2001**, *1*, 207–211.
- (33) Peng, X.; Manna, L.; Yang, W.; Wickham, J.; Scher, E.; Kadavanich, A.; Alivisatos, A. P. *Nature* **2000**, *404*, 59–61.
- (34) Battaglia, D.; Peng, X. *Nano Lett.* **2002**, *2*, 1027–1030.
- (35) Lappert, M. F.; Power, P. P.; Sanger, A. R.; Srivastava, R. C. *Metal and Metalloid Amides*; Ellis Horwood: Chichester, 1980.
- (36) Nayral, C.; Ould-Ely, T.; Maisonnat, A.; Chaudret, B.; Fau, P.; Lescouères, L.; Peyre-Lavigne, A. *Adv. Mater.* **1999**, *11*, 61–63.
- (37) Dumestre, F.; Chaudret, B.; Amiens, C.; Renaud, P.; Fejes, P. *Science* **2004**, *303*, 821–823.
- (38) Desvaux, C.; Amiens, C.; Fejes, P.; Renaud, P.; Respaud, M.; Lecante, P.; Snoeck, E.; Chaudret, B. *Nat. Mater.* **2005**, *4*, 750–753.
- (39) Lacroix, L.-M.; Lachaize, S. b.; Falqui, A.; Respaud, M.; Chaudret, B. *J. Am. Chem. Soc.* **2008**, *131*, 549–557.
- (40) Lacroix, L.-M.; Lachaize, S.; Falqui, A.; Blon, T.; Carrey, J.; Respaud, M.; Dumestre, F.; Amiens, C.; Margeat, O.; Chaudret, B.; Lecante, P.; Snoeck, E. *J. Appl. Phys.* **2008**, *103*, 07D521.
- (41) Meffre, A.; Lachaize, S.; Gatel, C.; Respaud, M.; Chaudret, B. *J. Mater. Chem.* **2011**, *21*, 13464–13469.
- (42) Klavetter, K. C.; Wood, S. M.; Lin, Y.-M.; Snider, J. L.; Davy, N. C.; Chockla, A. M.; Romanovicz, D. K.; Korgel, B. A.; Lee, J.-W.; Heller, A.; Mullins, C. B. *J. Power Sources* **2013**, *238*, 123–136.
- (43) Desvaux, C.; Dumestre, F.; Amiens, C.; Respaud, M.; Lecante, P.; Snoeck, E.; Fejes, P.; Renaud, P.; Chaudret, B. *J. Mater. Chem.* **2009**, *19*, 3268–3275.
- (44) Yarema, M.; Wörle, M.; Rossell, M. D.; Erni, R.; Caputo, R.; Protesescu, L.; Kravchyk, K. V.; Dirin, D. N.; Lienau, K.; von Rohr, F.; Schilling, A.; Nachtegaal, M.; Kovalenko, M. V. *J. Am. Chem. Soc.* **2014**, *136*, 12422–12430.
- (45) Yarema, M.; Kovalenko, M. V.; Hesser, G.; Talapin, D. V.; Heiss, W. *J. Am. Chem. Soc.* **2010**, *132*, 15158–15159.
- (46) Wang, F.; Tang, R.; Yu, H.; Gibbons, P. C.; Buhro, W. E. *Chem. Mater.* **2008**, *20*, 3656–3662.
- (47) Yarema, M.; Kovalenko, M. V.; Hesser, G.; Talapin, D. V.; Heiss, W. *J. Am. Chem. Soc.* **2010**, *132*, 15158–15159.
- (48) Yu, H.; Gibbons, P. C.; Kelton, K. F.; Buhro, W. E. *J. Am. Chem. Soc.* **2001**, *123*, 9198–9199.
- (49) Zhang, H.; Son, J. S.; Jang, J.; Lee, J.-S.; Ong, W.-L.; Malen, J. A.; Talapin, D. V. *ACS Nano* **2013**, *7*, 10296–10306.
- (50) Xu, X.; Cao, R.; Jeong, S.; Cho, J. *Nano Lett.* **2012**, *12*, 4988–4991.
- (51) Yarema, M.; Pichler, S.; Kriegner, D.; Stangl, J.; Yarema, O.; Kirchschlager, R.; Tollabimazraehno, S.; Humer, M.; Häring, D.; Kohl, M.; Chen, G.; Heiss, W. *ACS Nano* **2012**, *6*, 4113–4121.
- (52) Protesescu, L.; Rossini, A. J.; Kriegner, D.; Valla, M.; de Kergommeaux, A.; Walter, M.; Kravchyk, K. V.; Nachtegaal, M.; Stangl, J.; Malaman, B.; Reiss, P.; Lesage, A.; Emsley, L.; Coperet, C.; Kovalenko, M. V. *ACS Nano* **2014**, *8*, 2639–2648.
- (53) Koo, B.; Patel, R. N.; Korgel, B. A. *J. Am. Chem. Soc.* **2009**, *131*, 3134–3135.
- (54) Maier, J. *Chem. Mater.* **2014**, *26*, 348–360.
- (55) Li, N.; Song, H.; Cui, H.; Yanga, G.; Wang, C. *J. Mater. Chem. A* **2014**, *2*, 2526–2537.
- (56) Yuan, F.-W.; Tuan, H.-Y. *Chem. Mater.* **2014**, *26*, 2172–2179.
- (57) Wang, F.; Buhro, W. E. *Small* **2010**, *6*, 573–581.
- (58) Zolotavin, P.; Guyot-Sionnest, P. *ACS Nano* **2010**, *4*, 5599–5608.
- (59) Li, W.; Zamani, R.; Rivera Gil, P.; Pelaz, B.; Ibáñez, M.; Cadavid, D.; Shavel, A.; Alvarez-Puebla, R. A.; Parak, W. J.; Arbiol, J.; Cabot, A. J. *Am. Chem. Soc.* **2013**, *135*, 7098–7101.
- (60) Anderson, N. C.; Hendricks, M. P.; Choi, J. J.; Owen, J. S. *J. Am. Chem. Soc.* **2013**, *135*, 18536–18548.
- (61) Oliveira, M. J.; Gonze, X. *J. Phys. B* **2013**, *46*, 095101.
- (62) Grimme, S. *J. Comput. Chem.* **2006**, *27*, 1787–1799.
- (63) Mourdikoudis, S.; Liz-Marzáñ, L. M. *Chem. Mater.* **2013**, *25*, 1465–1476.
- (64) Palomares, V.; Serras, P.; Villaluenga, I.; Hueso, K. B.; Carretero-Gonzalez, J.; Rojo, T. *Energy Environ. Sci.* **2012**, *5*, 5884–5901.
- (65) Larcher, D.; Beattie, S.; Morcrette, M.; Edstrom, K.; Jumas, J.-C.; Tarascon, J.-M. *J. Mater. Chem.* **2007**, *17*, 3759–3772.
- (66) Ge, P.; Fouletier, M. *Solid State Ionics* **1988**, *28–30* (Part 2), 1172–1175.
- (67) Schwindeman, J. A.; Woltermann, C. J.; Letchford, R. J. *J. Chem. Health Saf.* **2002**, *9*, 6–11.
- (68) Jones, A. C.; Sanders, A. W.; Bevan, M. J.; Reich, H. J. *J. Am. Chem. Soc.* **2007**, *129*, 3492–3493.
- (69) Bruckner, R. *Organic mechanisms: reactions, stereochemistry and synthesis*; Springer: 2010.
- (70) Armstrong, D. R.; Carstairs, A.; Henderson, K. W. *Organometallics* **1999**, *18*, 3589–3596.
- (71) Henderson, K. W.; Williard, P. G. *Organometallics* **1999**, *18*, 5620–5626.
- (72) Lucht, B. L.; Collum, D. B. *J. Am. Chem. Soc.* **1994**, *116*, 6009–6010.
- (73) Lucht, B. L.; Collum, D. B. *Acc. Chem. Res.* **1999**, *32*, 1035–1042.
- (74) Lucht, B. L.; Collum, D. B. *J. Am. Chem. Soc.* **1995**, *117*, 9863–9874.
- (75) Lucht, B. L.; Bernstein, M. P.; Remenar, J. F.; Collum, D. B. *J. Am. Chem. Soc.* **1996**, *118*, 10707–10718.
- (76) Lucht, B. L.; Collum, D. B. *J. Am. Chem. Soc.* **1996**, *118*, 2217–2225.
- (77) Soulantica, K.; Maisonnat, A.; Fromen, M. C.; Casanove, M. J.; Lecante, P.; Chaudret, B. *Angew. Chem., Int. Ed.* **2001**, *40*, 448–451.
- (78) Nose, K.; Soma, Y.; Omata, T.; Otsuka-Yao-Matsuo, S. *Chem. Mater.* **2009**, *21*, 2607–2613.

- (79) Ghanta, S. R.; Rao, M. H.; Muralidharan, K. *Dalton Trans.* **2013**, *42*, 8420–8425.
- (80) Schutte, K.; Meyer, H.; Gemel, C.; Barthel, J.; Fischer, R. A.; Janiak, C. *Nanoscale* **2014**, *6*, 3116–3126.
- (81) Manthiram, K.; Beberwyck, B. J.; Alivisatos, A. P. *J. Am. Chem. Soc.* **2014**, *136*, 13319–13325.
- (82) Yang, H.-J.; He, S.-Y.; Chen, H.-L.; Tuan, H.-Y. *Chem. Mater.* **2014**, *26*, 1785–1793.
- (83) Jin, M.; He, G.; Zhang, H.; Zeng, J.; Xie, Z.; Xia, Y. *Angew. Chem., Int. Ed.* **2011**, *50*, 10560–10564.
- (84) Mayousse, C.; Celle, C.; Carella, A.; Simonato, J.-P. *Nano Res.* **2014**, *7*, 315–324.
- (85) Hung, L.-I.; Tsung, C.-K.; Huang, W.; Yang, P. *Adv. Mater.* **2010**, *22*, 1910–1914.
- (86) Mosby, J. M.; Prieto, A. L. *J. Am. Chem. Soc.* **2008**, *130*, 10656–10661.
- (87) Fransson, L. M.; Vaughney, J.; Benedek, R.; Edström, K.; Thomas, J. O.; Thackeray, M. *Electrochim. Commun.* **2001**, *3*, 317–323.
- (88) Wolfenstine, J.; Campos, S.; Foster, D.; Read, J.; Behl, W. *J. Power Sources* **2002**, *109*, 230–233.
- (89) Applestone, D.; Manthiram, A. *RSC Adv.* **2012**, *2*, 5411–5417.
- (90) Waggoner, K. M.; Power, P. P. *J. Am. Chem. Soc.* **1991**, *113*, 3385–3393.
- (91) Bosio, L. *J. Chem. Phys.* **1978**, *68*, 1221.
- (92) Bosio, L.; Defrain, A.; Epelboin, I. *J. Phys. - Paris* **1966**, *27*, 61–71.
- (93) Wang, F.; Dong, A.; Sun, J.; Tang, R.; Yu, H.; Buhro, W. E. *Inorg. Chem.* **2006**, *45*, 7511–7521.
- (94) Bennett, P. J.; Dhanjal, S.; Petropoulos, P.; Richardson, D. J.; Zheludev, N. I.; Emelyanov, V. I. *Appl. Phys. Lett.* **1998**, *73*, 1787.
- (95) Soares, B.; Jonsson, F.; Zheludev, N. *Phys. Rev. Lett.* **2007**, *98*, 153905.
- (96) Wu, P. C.; Khouri, C. G.; Kim, T.-H.; Yang, Y.; Losurdo, M.; Bianco, G. V.; Vo-Dinh, T.; Brown, A. S.; Everitt, H. O. *J. Am. Chem. Soc.* **2009**, *131*, 12032–12033.
- (97) Yang, Y.; Callahan, J. M.; Kim, T. H.; Brown, A. S.; Everitt, H. O. *Nano Lett.* **2013**, *13*, 2837–2841.
- (98) Vivekchand, S. R. C.; Engel, C. J.; Lubin, S. M.; Blaber, M. G.; Zhou, W.; Suh, J. Y.; Schatz, G. C.; Odom, T. W. *Nano Lett.* **2012**, *12*, 4324–4328.